

Hsin-Yeh Wu,<sup>1</sup> Marc Besançon,<sup>2</sup> Jia-Wern Chen,<sup>3</sup> Pisin Chen,<sup>1,4</sup> Jean-François Glicenstein,<sup>2</sup> Shu-Xiao Liu,<sup>1</sup> Yu-Jung Lu,<sup>1,3</sup> Xavier-François Navick,<sup>2</sup> Stathes Paganis,<sup>1,4, a)</sup> Boris Tuchming,<sup>2</sup> Dimitra Tsiou,<sup>1</sup> and Feng-Yang Tsai<sup>1,3</sup>

<sup>1)</sup>Department of Physics, National Taiwan University, Taipei 10617, Taiwan

<sup>2)</sup>CEA-IRFU, Paris-Saclay University 91190 Gif sur Yvette cedex, France

<sup>3)</sup>Research Center for Applied Sciences, Academia Sinica, Taipei 11529, Taiwan

<sup>4)</sup>Leung Center for Cosmology and Particle Astrophysics, National Taiwan University, Taipei 10617, Taiwan

(\*Electronic mail: paganis@phys.ntu.edu.tw)

(Dated: 15 October 2024)

A dual-operation mode SNSPD is demonstrated. In the conventional Geiger SNSPD mode the sensor operates at temperatures well below the critical temperature,  $T_C$ , working as an event counter without sensitivity to the number of photons impinging the sensor. In the calorimetric mode, the detector is operated at temperatures just below  $T_C$  and displays photon-number sensitivity for wavelengths in the optical spectrum. In this energy sensitive mode, photon absorption causes Joule heating of the SNSPD that becomes partially resistive without the presence of latching. Depending on the application, by tuning the sample temperature and bias current using the same readout system, the SNSPD can readily switch between the two modes. In the calorimetric mode, SNSPD recovery times shorter than the ones in the Geiger mode are observed, reaching values as low as 580 ps. Dual-mode SNSPD's may provide significant advancements in spectroscopy and calorimetry, where precise timing, photon counting and energy resolution are required.

## I. INTRODUCTION

During the past three decades, superconducting photon detector development has been advancing at a rapid pace. This progress is largely due to their low intrinsic energy threshold of order meV and dark-count rate (DCR) or noise equivalent power compared to traditional semiconductor photon detectors. Superconducting nanowire single-photon detectors (SNSPDs) are state-of-the-art single-photon sensors that have been widely adopted in various photonic applications. These applications include quantum key distribution (QKD)<sup>1</sup>, quantum information<sup>2</sup>, detection of luminescence from singlet oxygen<sup>3</sup>, LiDAR applications<sup>4</sup> and more. SNSPDs exhibit several outstanding characteristics: near 100% system detection efficiency<sup>5,6</sup>, excellent timing resolution with low timing jitter<sup>6</sup>, extremely low DCR, very high count rate, and a broad spectral operating range<sup>7</sup>.

Conventional SNSPD operation temperatures,  $T_{op}$ , are well below the superconducting critical temperature,  $T_C$ . The detectors are biased with a direct bias current just below the switching current (defined as the current at which the SNSPD starts becoming resistive),  $I_{sw}(T)$ . Absorption of photons induce local hotspots in the nanowires that extend in the full width of the wire, causing the bias current density to exceed the critical current density and trigger a transition from the superconducting state to the normal-conducting state. This process enables SNSPDs to operate in a single-photon counting mode<sup>8</sup>. While SNSPDs are highly effective in the single-photon counting (Geiger) mode, they are not sensitive to the number of photons impinging the detector, or equivalently, they are not energy sensitive. There have been attempts to fabricate photon-number-resolving SNSPDs, where multiple photons create multiple local hotspots, inducing different dis-

crete resistance changes<sup>9,10</sup>. However, the dynamic range of these devices remains limited.

In contrast, other types of superconducting detectors, such as transition-edge sensors (TES) and microwave kinetic inductance detectors (MKID), offer microcalorimeter capabilities. These devices provide good energy resolution by measuring the temperature rise or changes in the surface impedance of a superconductor through the kinetic inductance effect induced by photon absorption. This allows for precise energy measurements. However, despite their good energy resolution, TES and MKID detectors typically exhibit slower response times compared to SNSPDs<sup>11,12</sup>. This trade-off between energy resolution and timing capability is a critical consideration when selecting the appropriate detector for specific applications.

Several newly proposed experiments that employ single-photon sensors, require energy resolution and stringent timing capabilities, including precise timing resolution and minimal timing jitter, with a very low DCR. For instance, the AnABEL (Analog Black Hole Evaporation via Lasers) experiment<sup>13</sup> aims to detect entangled photon pairs from Hawking-analogue radiation produced by accelerating plasma mirrors. This experiment demands very low timing jitter and high timing resolution to distinguish the entangled photon pairs from the irreducible photon background generated by the laser plasma. Good energy resolution is also required to validate the blackbody radiation energy spectrum of the Hawking photons. Another relevant research initiative is the next generation of neutrinoless double-beta decay experiments, such as CUPID (CUORE Upgrade with Particle IDentification)<sup>14</sup>, where one needs to resolve an irreducible background to two-neutrino double-beta decay ( $2\nu\beta\beta$ ) events from scintillating crystals. These background events contribute to the experiment as pileup, necessitating excellent timing resolution in order to resolve them. Furthermore, quantum information and quantum key distribution experiments, aiming at high repetition rates exceeding GHz<sup>1,15</sup>, impose stringent timing require-

<sup>a)</sup><https://tidc.phys.ntu.edu.tw/>

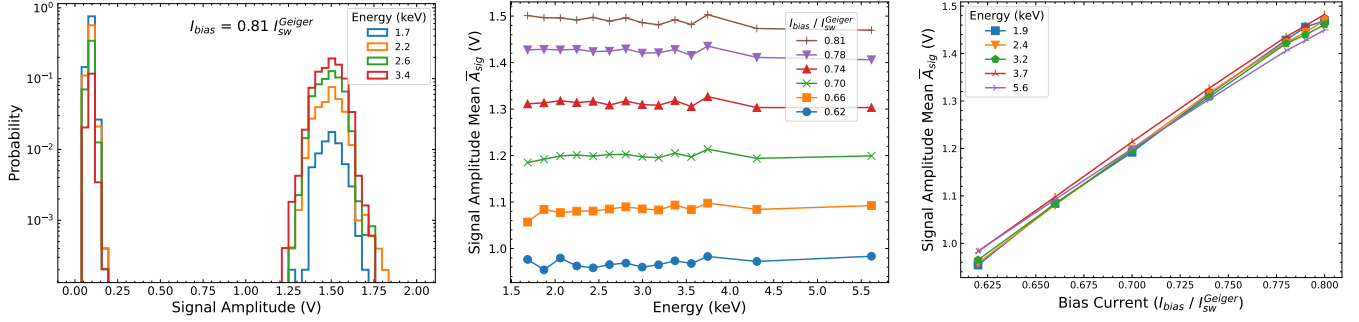


FIG. 1. Geiger mode: The SNSPD is operated at 4.68K ( $0.39 T_C$ ). Left: Recorded signal amplitude distributions for different laser energies normalized to unity, for a bias current set at  $0.81 I_{sw}^{Geiger}$ . Middle: Signal amplitude mean as a function of the bias current, for a range of laser energies. Right: Signal amplitude mean as a function of the bias current, for a range of laser energies. The lines connecting the data points serve as visual guides to illustrate the trends.

ments on the photon detectors.

The conventional SNSPD single-photon operation mode (the Geiger mode) leads to pulse amplitudes that are constant, independent of the number of photons impinging the sensor. The widely accepted physics mechanism behind this behaviour is due to vortex crossing from one side of the wire to the other and vortex-vortex annihilation in the center of the wire<sup>16</sup>. In this mode the wire is biased at relatively high bias current of order  $100 \mu\text{A}$  increasing the probability of vortex-crossing. After photon absorption, the formation of a hot spot reduces the potential barrier for vortex crossing and leads to the rapid growth of the hot spot region to the whole width of the wire. This process has been shown<sup>16</sup> to result to pulse amplitudes independent of the number of photons absorbed by the sensor.

In this work, we explore a high-speed calorimetric operation mode of SNSPD, where the detector is now sensitive to the number of absorbed photons. When the SNSPD is operated just below the  $T_C$ , the switching current  $I_{sw}^{Cal}$  is an order of magnitude lower than the one in the Geiger mode. Operating the detector at a bias current close to  $I_{sw}^{Cal}$  leads to suppression of vortex crossing. Absorption of photons does not induce vortex crossing but instead leads to joule heating of the SNSPD that becomes partially resistive with the resistance of the wire and thus the amplitude of the observed pulses increasing with the number of absorbed photons.

In the following sections we demonstrate the dual-operation mode of SNSPDs: (i) a *Geiger* single-photon or multi-photon event counting mode and (ii) a photon-number sensitive *calorimetric* mode. This dual-mode capability allows the SNSPD to switch between high-precision event counting and energy measurement by adjustment of  $I_{bias}$  and  $T_{Op}$ , thus offering a versatile solution for high-speed spectroscopy applications.

## II. SNSPD FABRICATION AND EXPERIMENTAL SETUP

The first step of the fabrication process of the SNSPDs used in this work, is the deposition of 15 nm NbN thin films on

MgO substrates using RF sputtering under the following conditions: 120 W power, 36:0.1 sccm Ar:N<sub>2</sub> flow rate, 0.9 mTorr pressure, and a substrate temperature of 800°C. For more detailed information on the NbN thin film characterization, the reader should refer to Ref. 17 and its supporting documentation. The films are subsequently patterned into a nanowire meander structure using electron-beam lithography (EBL) with ZEP520A resist mixed with ZEP-A at a 1:1 ratio, and developed with ZED-N50 developer. The nanowire meander has a width of 200 nm, a pitch of 350 nm, and a total length of 684  $\mu\text{m}$ , covering a sensing area of 12  $\mu\text{m}$  by 12  $\mu\text{m}$ . The structure is etched using reactive ion etching with a CF<sub>4</sub>:O<sub>2</sub> flow rate of 20:2 sccm and a DC power of 200 W. The critical temperature ( $T_C$ ) of the SNSPD was measured to be 12 K.

During characterization and testing, the SNSPD is mounted on the 4K stage of a pulse-tube cryocooler with custom-made packaging. In this work, we adopt two operating temperatures to demonstrate the two distinct operating modes: The first is the Geiger mode at 4.68 K ( $0.39 T_C$ ), characterized by a switching current,  $I_{sw}^{Geiger}$ , of 127  $\mu\text{A}$  and a superconducting transition width of 1 nA, indicating a sharp superconducting transition. The second is the calorimetric mode operated at 11.47 K ( $0.96 T_C$ ), with a switching current,  $I_{sw}^{Cal}$ , of 12.5  $\mu\text{A}$  and a superconducting transition width of 48  $\mu\text{A}$ , indicating a slow and wide superconducting transition. In this mode, the SNSPD can operate both in the superconducting state with  $I_{bias}$  below  $I_{sw}^{Cal}$ , or in a partially resistive state with  $I_{bias}$  above  $I_{sw}^{Cal}$  before fully transitioning to the non-superconducting state. The reader should refer to *Supplementary Material* for more information on the resistance-current diagram of this sample.

During SNSPD photoresponse measurements, we employ a picosecond pulsed laser (Prima from PicoQuant) featuring three visible wavelengths, a pulse width of less than 100 ps, and a variable repetition rate ranging from 1 kHz to 200 MHz. We select a 515 nm wavelength as our primary source. The laser is coupled to the SNSPD sensing area through open air, with the laser spot size focused to a diameter of 3  $\mu\text{m}$ . The SNSPD is biased through a bias tee (Minicircuits ZFBT-4R2GW+), and output signal pulses are amplified using two

room-temperature low-noise amplifiers (RFBay LNA-1030, with a bandwidth of 20 MHz to 1 GHz, 30 dB gain, and a noise figure of 1.3 dB). The amplified signal is digitized by a PXI Express Oscilloscope with an external trigger from the pulsed laser (NI PXIe-5162, featuring 1.5 GHz bandwidth, 2.5 GS/s per channel sampling rate, and an effective number of bits of 7.0 at 50Ω). A data acquisition gate of 1000 time samples (400 ns) is set for each laser trigger, with the trigger reference position at 30%. This setup, typically used for a pulsed-laser repetition rate of 10 kHz, covers a single signal pulse with a duration of approximately 40 ns and a measured latency of 20 ns with respect to the trigger time of arrival. We define as laser energy,  $E_{Laser}$ , the expected energy per laser pulse after taking into account the measured attenuation from the point of emission to the sensor surface.  $E_{Laser}$  is the energy equivalent of the number of photons impinging the sensor without any photon absorption efficiency correction applied. The detailed experimental setup and example signal-pulse spectra are presented in the *Supplementary Material*.

### III. RESULTS

In the following, we present the results obtained with the SNSPD operating at two different temperatures. First, for 0.39  $T_C$  in the Geiger mode, the dependence of the signal pulse amplitude,  $A_{sig}$ , on the expected energy per laser pulse  $E_{Laser}$  and  $I_{bias}$  is shown in Fig. 1. The amplitude  $A_{sig}$  of each laser pulse is measured offline and defined as the pulse peak-to-peak voltage difference within a fixed 25 ns time gate. This gate starts 1 ns before the triggered signal-pulse arrival, to approximately 10 ns after the lowest level of the overshoot from a typical signal pulse as shown in the *Supplementary Material*. The timing jitter of the signal pulses is shorter than the sampling rate, leading to a negligible probability of the fixed gate to miss the signal.

Fig. 1(left) shows the amplitude,  $A_{sig}$ , distributions (normalized to unity) at different laser energies for a  $I_{bias}$  of 0.81  $I_{sw}^{Geiger}$ . To extract these amplitudes for each energy, 10,000 pulsed-laser triggers are used. There are two distinct groups of events for each intensity: the signal events, peaked at 1.44 V, representing the fraction of absorbed-photon signal pulses that coincide with the laser trigger, and the noise events, peaked at 0.1 V, representing the fraction of events producing no SNSPD signal. In this case,  $A_{sig}$  corresponds to the peak-to-peak amplitude of the electronic noise. As  $E_{Laser}$  increases, the fraction of the signal events increases, while the average amplitude of the signal distribution is constant, indicating that  $E_{Laser}$  correlates to the laser pulse detection efficiency but not to the signal amplitude mean,  $\bar{A}_{sig}$ .  $\bar{A}_{sig}$  is obtained by a Gaussian fit of the signal peak. Fig. 1(middle) displays the dependence of the signal amplitude mean to the laser energy,  $E_{Laser}$ , for different settings of the bias current,  $I_{bias}$ . As expected for an SNSPD operating in the Geiger mode for fixed bias current, no dependence of the signal amplitude on the laser energy is observed. In Fig. 1(right) the dependence of the amplitude mean to the normalized bias current for fixed  $E_{Laser}$  is shown. A linear correlation between  $\bar{A}_{sig}$

and  $I_{bias}$  is observed.

In the calorimetric mode, where the SNSPD is operated at 0.96  $T_C$ , the signal amplitude distribution and means are shown in Fig. 2. In Fig. 2(left), the amplitude distributions (normalized to unity) are shown for a bias current  $I_{bias}$  at 0.95  $I_{sw}^{Cal}$  and different laser energies,  $E_{Laser}$ . In this mode, all events recorded are signal events, while for higher laser energy the Gaussian-shape amplitude distributions shift to higher values. The dependence of the amplitude mean,  $\bar{A}_{sig}$ , on  $E_{Laser}$  for different bias currents,  $I_{bias}$ , is presented in Fig.2(middle). The amplitude mean increases non-linearly with  $E_{Laser}$ , with the increase being slower at high laser energies. The amplitude is maximum for bias currents just below the switching current. At lower energy levels, there is a region where  $\bar{A}_{sig}$  is almost constant, indicating that the SNSPD signal amplitude is smaller than the electronic noise and  $\bar{A}_{sig}$  becomes noise-dominated. The dependence of the signal amplitude mean on the bias current for different laser energies, is shown in Fig.2(right). For all energies, an initial increase of the amplitude with  $I_{bias}$  is observed until the bias current reaches the switching current. Beyond this point,  $\bar{A}_{sig}$  begins to decrease, due to the partial transition of the SNSPD from the superconducting to the resistive state.

In addition to the pulse amplitude, a pulse-shape analysis is performed. The pulse shape also exhibits differences when comparing the Geiger with the calorimetric mode. Fig. 3 displays the pulse shapes, averaged over 1000 signal pulses to mitigate electric noise contributions. The averaged shapes are shown for different  $I_{bias}$  values at a fixed  $E_{Laser}$  for the two operation modes. The pulse falling time constant,  $\tau_{fall}$ , indicates the time the bias current needs to return from the load resistance to the SNSPD. The load resistance,  $R_L$ , the SNSPD resistance,  $R_{SNSPD}$ , and the SNSPD kinetic inductance,  $L_k$ , are related by the formula:  $\tau_{fall} = L_k / (R_L + R_{SNSPD})$ .  $\tau_{fall}$  is obtained by performing an exponential fit to the falling edge of the pulse, using the expression:  $Ae^{-(t-t_0)/\tau_{fall}} + C$ . In the Geiger mode, the signal pulse shapes exhibit an amplitude increasing with the bias current, while the superconducting state pulse falling time,  $\tau_{fall}^{sc}$ , remains approximately constant at a value of 2.43 ns. For this constant  $\tau_{fall}^{sc}$  and  $R_L = 50 \Omega$ ,  $R_{SNSPD} = 0 \Omega$ , a kinetic inductance  $L_k$  of 121.5 nH, is extracted. In the calorimetric mode, the falling time,  $\tau_{fall}^{res}$ , is longer than the constant  $\tau_{fall}^{sc}$  for bias currents below the switching current  $I_{sw}^{Cal}$ . It decreases linearly with increasing bias current and becomes smaller than  $\tau_{fall}^{sc}$  above  $I_{sw}^{Cal}$ . For these measurements, the kinetic inductance decreases with a rate of 470 nH/ $\mu$ A. For larger values of bias current, the time constant decreases non-linearly approaching a saturation value of approximately 580 ps. As  $R_{SNSPD}$  is no longer zero but increasing non-linearly with  $I_{bias}$ , the saturated  $\tau_{fall}^{res}$  indicates a non-linear increase in  $L_k$ . Notably, operating with  $I_{bias}$  above  $I_{sw}^{Cal}$  provides a faster reset time compared to the conventional Geiger mode. As detailed in the *Supplementary Material* where plots of  $\tau_{fall}$  at different  $E_{Laser}$  in both modes are presented,  $\tau_{fall}$  does not show strong dependence on  $E_{Laser}$ .

Finally, it is important to note that while operating in

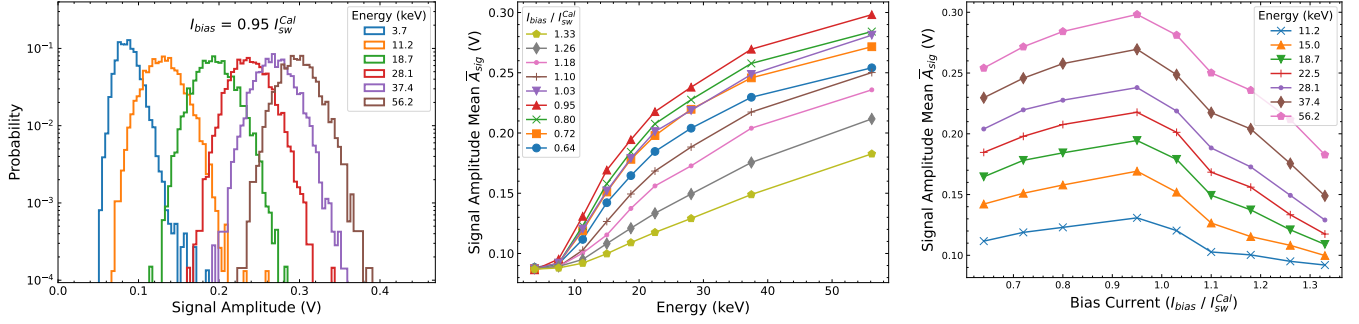


FIG. 2. Calorimetric Mode: The SNSPD is operated at 11.47K ( $0.96 T_C$ ). Left: Example probability distribution of the signal amplitude when operating with  $I_{bias}$  at  $0.95 I_{sw}^{Cal}$ . The distribution shifts with  $E_{Laser}$ , demonstrating the energy dependence of the signal amplitude. Middle: Profile of the signal amplitude mean as a function of pulse laser energy under different  $I_{bias}$  values. Right: Profile of the signal amplitude mean as a function of  $I_{bias}$  under different pulse laser energy levels. The lines serve as visual guides to illustrate the trends.

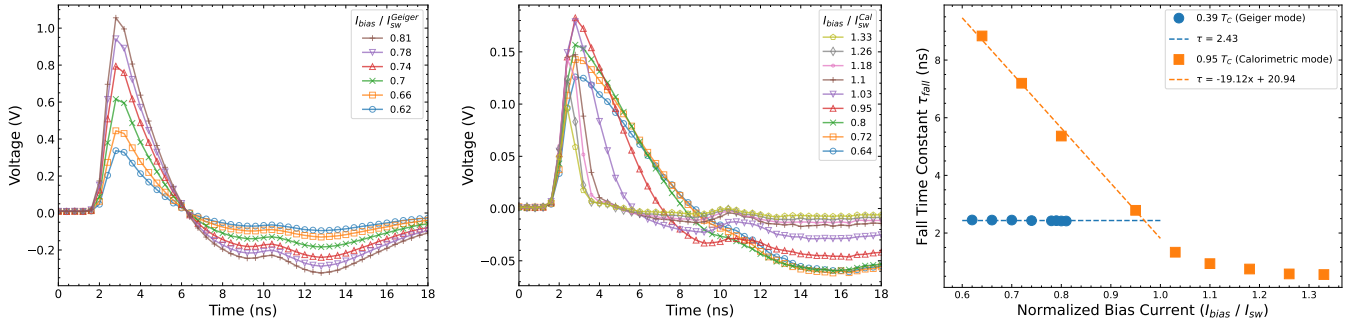


FIG. 3. Sample SNSPD signal spectra, averaged over 1000 laser events at a fixed  $E_{Laser}$  for a range of bias currents, are shown to illustrate the characteristics of the Geiger mode (left) and Calorimetric mode (middle). In these spectra, the markers represent the digitized samples, while the lines serve as a visual guide. An undershoot in the spectrum is evident due to the bandwidth limitations of the low-noise amplifiers. In the right panel the fitted-pulse time constant ( $\tau_{fall}$ ) is presented as a function of the normalized bias current  $I_{bias}/I_{sw}^{Geiger}$  for both Geiger and Calorimetric modes. For the Geiger mode, the data are shown up to  $0.81 I_{sw}^{Geiger}$ , as the SNSPD latches above this bias current. For data points corresponding to bias currents smaller than the switching current,  $I_{sw}(T)$ , the results of two linear fits are also shown.

the calorimetric mode, the DCR was measured using self-triggering and was found to be negligible.

#### IV. DISCUSSION

From the results presented in the previous section, it is clear that in the calorimetric mode the measured signal is due to a different physical mechanism than in the case of the conventional Geiger mode. In both modes, the absorbed photons trigger a sudden increase in the SNSPD resistance that redirects the bias current to the load resistance, resulting in an output signal pulse<sup>18</sup>. In the Geiger mode, the SNSPD resistance transitions from zero to a large constant value corresponding to the resistance of the normal conducting state. The measured resistance of the SNSPD conducting state is approximately 300 k $\Omega$ . Since this transition leads to a constant jump of the SNSPD resistance, a constant signal amplitude for a fixed  $I_{bias}$  is observed. Variations in  $I_{bias}$  lead to a linear change in signal amplitude, consistent with the results presented in Fig. 1.

In the calorimetric mode the behaviour of the signal amplitude and the pulse shape suggest a Joule heating mechanism in action. This mechanism dominates the vortex-crossing mechanism that is considered to be responsible for the Geiger operation mode. One reason for the suppression of vortex crossing is due to the bias current in the calorimetric mode being an order of magnitude lower than that in the Geiger mode. Assuming the same electrical model for both modes, when operating in the calorimetric mode, after the absorption of a certain amount of energy the nanowire experiences a partial transition to the resistive state. The absorbed photons cause Joule heating in the SNSPD leading to an increase in the SNSPD resistance. At high laser energies or equivalently high photon numbers absorbed, the SNSPD is expected to become fully resistive and approach a resistance of 300 k $\Omega$ . As shown in Fig. 4, what we actually measure is an amplitude that approaches saturation at a value consistent with the bias current and the 50 Ohm load resistance. It is important to note that the typical bias currents in the calorimetric mode are significantly lower than the ones in the Geiger mode, thus the corresponding signal pulse amplitudes are also lower. If the

SNSPD is operated with a bias current above  $I_{sw}(T)$ , the signal amplitude decreases, as expected, since the initial state of the SNSPD is already partially resistive.

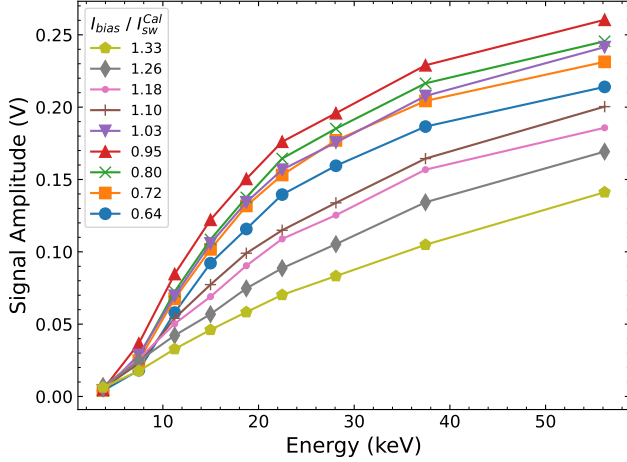


FIG. 4. Signal pulse amplitude mean,  $\bar{A}_{sig}$ , as a function of laser energy in the calorimetric mode. Unlike Fig.1(middle), where  $\bar{A}_{sig}$  is measured directly from individual laser events, here  $\bar{A}_{sig}$  is obtained by averaging over 1000 pulsed-laser events to reduce electronic noise, and subsequently measuring the peak-to-peak voltage range of the averaged pulse spectrum. This approach mitigates the inefficiency at low  $E_{Laser}$  due to a poor signal-to-noise ratio, thereby improving the behaviour of the amplitude mean observed at low  $E_{Laser}$  in Fig.1(middle). The lines connecting the data points in the plot serve as visual guides.

The sensitivity of the SNSPD to the number of absorbed photons when the detector is exposed in a pulsed-laser beam of fixed wavelength, allows measurements at small photon numbers or equivalently small energies. However, such measurements are limited by the noise level in our setup. The effect of the noise can be observed in the signal amplitude mean shown in Fig. 2. By averaging the output signal spectrum over 1000 events and measuring the peak-to-peak voltage range, it is evident that the SNSPD is sensitive to low energies corresponding to few-photon pulses, as demonstrated in Fig. 4. The fractional energy resolution defined as the ratio of the standard deviation of a Gaussian fit of the signal amplitude distribution divided by the amplitude mean,  $\sigma/\bar{A}$ , is presented in Fig. 5 for different laser energies and for different bias currents. The fractional resolution is modeled using the expression  $\sqrt{((A/E)^2 + (B/\sqrt{E})^2 + C^2)}$ , where A corresponds to the noise term, B the stochastic term, and C the constant term. Fits of the data with this model for three different  $I_{bias}$  are also shown in Fig. 5. For bias currents close to the switching current where the amplitude is maximum we observe a resolution around 10% for high energies, while for low energies where the noise contribution dominates, the 0.95  $I_{bias}$  selection gives the best resolution. The large contribution from noise in these measurements suggests that improving the signal-to-noise ratio in the electronics readout system is a key to optimizing the performance of dual-mode SNSPDs.

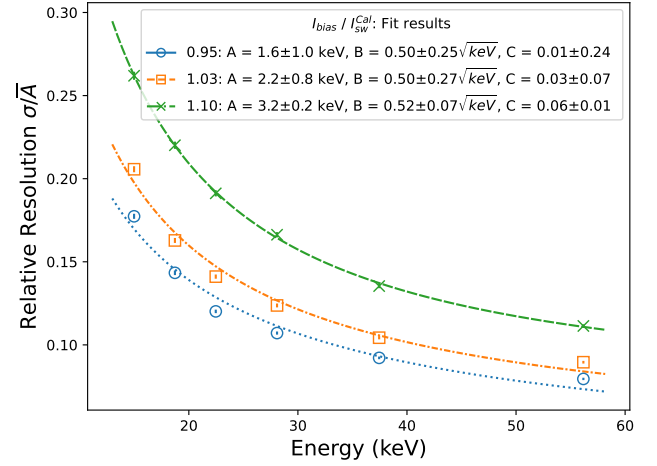


FIG. 5. SNSPD energy resolution in the calorimetric mode for 3 sample bias currents. In the  $x$ -axis, energy corresponds to the attenuated laser energy, but it does not include the sensor photon absorption efficiency. The results of fits using a resolution model discussed in the text, are shown in dotted lines. The results of these fits are presented in the legend, where A represents the noise term, B the stochastic term, and C the constant term of the resolution model.

An additional difference between the two operating modes is observed in the effect of latching. Latching occurs when the time needed for the bias current to return from the load to the SNSPD is shorter than the SNSPD self-reset time, preventing the SNSPD from returning to its original operating state<sup>19</sup>. In the Geiger mode, latching is observed near  $I_{sw}^{Geiger}$ , while in the calorimetric mode, latching does not occur for any  $I_{bias}$  (above or below  $I_{sw}^{Cal}$ ). This demonstrates the stable operation of the SNSPD in the calorimetric mode, even when the current return time is shorter than in the Geiger mode. In addition, the timing jitter was measured to be approximately 108 ps using a Time-Correlated Single-Photon Counting module with a 4 ps timing resolution. It is important to note that the pulsed-laser width of 100 ps and the electronic noise were not subtracted from the timing jitter measurement, so the internal timing jitter of the SNSPD is expected to be less than 108 ps. Furthermore, the DCR is low in both modes, approximately 1 count per minute in the Geiger mode, while no dark counts are observed in the calorimetric mode.

The calorimetric behaviour of the SNSPD is analogous to the mechanism described in transition edge sensors (TES)<sup>20</sup>, where the resistance of the superconducting nanowire changes due to variations in temperature and current density from photon absorption. However, there are several performance differences between the calorimetric SNSPD and other cryogenic calorimeters, summarized in Table I. The timing capability of the calorimetric SNSPD is a significant advantage, offering fast  $\tau_{fall}$  for quick recovery times of the detection system and small timing jitter. The single-photon or a few-photon sensitivity of SNSPDs is another advantage. However, the energy resolution of the calorimetric SNSPD developed in this study is still electronic-noise limited.

The primary challenges for the calorimetric mode include



TABLE I. A comparison of the SNSPD in the Calorimetric mode presented in this work with state-of-the-art cryogenics bolometers.

Detectors	$\sigma/E$	$\tau_{fall}$	Timing Jitter
TES <sup>11,21</sup>	0.06% (@1 keV)	87 $\mu$ s	10-100 ns
MKID <sup>12,22</sup>	1.8% (@3 eV)	32 $\mu$ s	-
NTD-Ge <sup>14,23</sup>	0.1% (@6 keV)	7 ms	-
Calorimetric SNSPD	<6% const. term	580 ps	< 108 ps

demonstrating single-photon sensitivity with high efficiency and obtaining high-energy resolution for wavelength spectroscopy at the eV level, which would enable fast spectroscopy. Currently, a major issue in our system is external electrical noise, which could be mitigated by employing low-noise cryogenic amplifiers and improving the cryogenic system to be noise-free. Future work should also explore the effects of nanowire geometry. In this study, we used a 15 nm thick, 200 nm wide NbN nanowire due to its higher  $T_C$ , because the main goal is to explore the dual-mode operation at different temperatures, and such dimensions simplify our setup in the available cryogenic system. In this particular nanowire design, the wire is thicker and wider compared to those used in fabricating high-efficiency SNSPDs. Exploring thinner and narrower nanowire geometries is expected to enhance sensitivity. In addition, incorporating optical structures such as mirrors or cavities will further optimize the detector performance.

## V. CONCLUSIONS

A dual-mode SNSPD operating in both the conventional Geiger mode and the calorimetric mode is demonstrated. The SNSPD is tested and readout in an external-trigger mode using a pulsed laser emitting photons in the visible range. Depending on the application, by tuning the sample temperature and bias current using the same readout system, the SNSPD can readily switch between the Geiger mode for single-photon counting and calorimetric mode for sensitivity to the number of monochromatic photons or energy. This dual-mode capability is enhanced by a low DCR, stable operation in the calorimetric mode, and a relatively simple fabrication process. At high energies an energy resolution better than 10% is observed, although at lower energies the resolution performance is limited due to electronic noise. The fast timing capability of these SNSPDs and the dual-mode operation show potential for high-speed spectroscopy and other applications requiring precise timing measurements.

## SUPPLEMENTARY MATERIAL

See the *Supplementary Material* for detailed information of the resistance-current diagram and experimental setups.

## ACKNOWLEDGMENTS

We wish to acknowledge the support of the NTU-Saclay Joint Laboratory for Infrared Quantum single photon Sensors (IQSENS) grant. This work has been supported in part by the LabEx FOCUS grant, ANR-11-LABX-0013. The authors would like to thank Stefanos Marnieros and Matias Rodrigues for preparing and establishing the electric contacts on certain SNSPDs. NbN film  $T_C$  measurements were performed using a SQUID at CCMS, NTU, by Li-Min Wang and his group.

## DATA AVAILABILITY STATEMENT

The data that support the findings of this study are available from the corresponding author upon request.

- <sup>1</sup>F. Beutel, H. Gehring, M. A. Wolff, C. Schuck, and W. Pernice, "Detector-integrated on-chip QKD receiver for GHz clock rates," *npj Quantum Information* **7**, 1–8 (2021).
- <sup>2</sup>L. You, "Superconducting nanowire single-photon detectors for quantum information," *Nanophotonics* **9**, 2673–2692 (2020).
- <sup>3</sup>N. R. Gemmill, A. McCarthy, B. Liu, M. G. Tanner, S. D. Dorenbos, V. Zwiller, M. S. Patterson, G. S. Buller, B. C. Wilson, and R. H. Hadfield, "Singlet oxygen luminescence detection with a fiber-coupled superconducting nanowire single-photon detector," *Optics Express* **21**, 5005–5013 (2013).
- <sup>4</sup>G. G. Taylor, D. Morozov, N. R. Gemmill, K. Erotokritou, S. Miki, H. Terai, and R. H. Hadfield, "Photon counting LIDAR at 2.3 $\mu$ m wavelength with superconducting nanowires," *Optics Express* **27**, 38147–38158 (2019).
- <sup>5</sup>D. V. Reddy, R. R. Nerem, S. W. Nam, R. P. Mirin, and V. B. Verma, "Superconducting nanowire single-photon detectors with 98% system detection efficiency at 1550 nm," *Optica* **7**, 1649 (2020).
- <sup>6</sup>J. Chang, J. W. N. Los, J. O. Tenorio-Pearl, N. Noordzij, R. Gourgues, A. Guardiani, J. R. Zichi, S. F. Pereira, H. P. Urbach, V. Zwiller, S. N. Dorenbos, and I. Esmail Zadeh, "Detecting telecom single photons with 99.5-2.07+0.5% system detection efficiency and high time resolution," *APL Photonics* **6**, 036114 (2021).
- <sup>7</sup>I. Esmail Zadeh, J. Chang, J. W. N. Los, S. Gyger, A. W. Elshaari, S. Steinhauer, S. N. Dorenbos, and V. Zwiller, "Superconducting nanowire single-photon detectors: A perspective on evolution, state-of-the-art, future developments, and applications," *Applied Physics Letters* **118**, 190502 (2021).
- <sup>8</sup>A. Engel, J. J. Renema, K. Il'in, and A. Semenov, "Detection mechanism of superconducting nanowire single-photon detectors," *Superconductor Science and Technology* **28**, 114003 (2015).
- <sup>9</sup>C. Cahall, K. L. Nicolich, N. T. Islam, G. P. Lafyatis, A. J. Miller, D. J. Gauthier, and J. Kim, "Multi-photon detection using a conventional superconducting nanowire single-photon detector," *Optica* **4**, 1534–1535 (2017).
- <sup>10</sup>D. Zhu, M. Colangelo, C. Chen, B. A. Korzh, F. N. C. Wong, M. D. Shaw, and K. K. Berggren, "Resolving Photon Numbers Using a Superconducting Nanowire with Impedance-Matching Taper," *Nano Letters* **20**, 3858–3863 (2020).
- <sup>11</sup>M. D. Eisaman, J. Fan, A. Migdall, and S. V. Polyakov, "Invited Review Article: Single-photon sources and detectors," *Review of Scientific Instruments* **82**, 071101 (2011).
- <sup>12</sup>N. Swimmer, W. H. Clay, N. Zobrist, and B. A. Mazin, "Characterizing the dark count rate of a large-format MKID array," *Optics Express* **31**, 10775–10793 (2023).
- <sup>13</sup>P. Chen, G. Mourou, M. Besancon, Y. Fukuda, J.-F. Glicenstein, J. Nam, C.-E. Lin, K.-N. Lin, S.-X. Liu, Y.-K. Liu, M. Kando, K. Kondo, S. Paganis, A. Pirozhkov, H. Takabe, B. Tuchming, W.-P. Wang, N. Watanura, J. Wheeler, and H.-Y. Wu, "AnaBHEL (Analog Black Hole Evaporation via Lasers) Experiment: Concept, Design, and Status," *Photonics* **9**, 1003 (2022).
- <sup>14</sup>CUPID collaboration, K. Alfonso, *et al.*, "A first test of CUPID prototypical light detectors with NTD-Ge sensors in a pulse-tube cryostat," *Jour-*

- nal of Instrumentation **18**, P06033 (2023), arXiv:2304.04674 [nucl-ex, physics:physics].
- <sup>15</sup>M. Anderson, T. Müller, J. Skiba-Szymanska, A. B. Krysa, J. Huwer, R. M. Stevenson, J. Heffernan, D. A. Ritchie, and A. J. Shields, “Gigahertz-Clocked Teleportation of Time-Bin Qubits with a Quantum Dot in the Telecommunication C Band,” *Physical Review Applied* **13**, 054052 (2020).
- <sup>16</sup>L. N. Bulaevskii, M. J. Graf, C. D. Batista, and V. G. Kogan, “Vortex-induced dissipation in narrow current-biased thin-film superconducting strips,” *Physical Review B* **83** (2011), 10.1103/physrevb.83.144526.
- <sup>17</sup>J.-W. Yang, T.-Y. Peng, D. D. A. Clarke, F. D. Bello, J.-W. Chen, H.-C. Yeh, W.-R. Syong, C.-T. Liang, O. Hess, and Y.-J. Lu, “Nanoscale Gap-Plasmon-Enhanced Superconducting Photon Detectors at Single-Photon Level,” *Nano Letters* (2023), 10.1021/acs.nanolett.3c01703.
- <sup>18</sup>J. K. W. Yang, A. J. Kerman, E. A. Dauler, V. Anant, K. M. Rosfjord, and K. K. Berggren, “Modeling the Electrical and Thermal Response of Superconducting Nanowire Single-Photon Detectors,” *IEEE Transactions on Applied Superconductivity* **17**, 581–585 (2007).
- <sup>19</sup>A. J. Annunziata, O. Quaranta, D. F. Santavica, A. Casaburi, L. Frunzio, M. Ejrnaes, M. J. Rooks, R. Cristiano, S. Pagano, A. Frydman, and D. E. Prober, “Reset dynamics and latching in niobium superconducting nanowire single-photon detectors,” *Journal of Applied Physics* **108**, 084507 (2010).
- <sup>20</sup>J. N. Ullom and D. A. Bennett, “Review of superconducting transition-edge sensors for x-ray and gamma-ray spectroscopy\*,” *Superconductor Science and Technology* **28**, 084003 (2015).
- <sup>21</sup>K. M. Morgan, D. T. Becker, D. A. Bennett, W. B. Doriese, J. D. Gard, K. D. Irwin, S. J. Lee, D. Li, J. A. B. Mates, C. G. Pappas, D. R. Schmidt, C. J. Titus, D. D. Van Winkle, J. N. Ullom, A. Wessels, and D. S. Swetz, “Use of Transition Models to Design High Performance TESs for the LCLS-II Soft X-Ray Spectrometer,” *IEEE Transactions on Applied Superconductivity* **29**, 1–5 (2019).
- <sup>22</sup>M. De Lucia, G. Ulbricht, E. Baldwin, J. D. Piercy, O. Creaner, C. Bracken, and T. P. Ray, “Limitations to the energy resolution of single-photon sensitive microwave kinetic inductance detectors,” *AIP Advances* **13**, 125026 (2023).
- <sup>23</sup>S. Bandler, E. Silver, H. Schnopper, S. Murray, M. Barbera, N. Madden, D. Landis, J. Beeman, Eugene Haller, and G. Tucker, “NTD-GE-based microcalorimeter performance,” *Nuclear Instruments and Methods in Physics Research Section A: Accelerators, Spectrometers, Detectors and Associated Equipment* **444**, 273–277 (2000).

# Dual Mode Superconducting Nanowire Single Photon Detectors: Supplementary Materials

Hsin-Yeh Wu,<sup>1</sup> Marc Besançon,<sup>2</sup> Jia-Wern Chen,<sup>3</sup> Pisin Chen,<sup>1,4</sup> Jean-François Glicenstein,<sup>2</sup> Shu-Xiao Liu,<sup>1</sup> Yu-Jung Lu,<sup>1,3</sup> Xavier-François Navick,<sup>2</sup> Stathes Paganis,<sup>1,4, a)</sup> Boris Tuchming,<sup>2</sup> Dimitra Tsionou,<sup>1</sup> and Feng-Yang Tsai<sup>1,3</sup>

<sup>1)</sup>*Department of Physics, National Taiwan University, Taipei 10617, Taiwan*

<sup>2)</sup>*CEA-IRFU, Paris-Saclay University 91190 Gif sur Yvette cedex, France*

<sup>3)</sup>*Research Center for Applied Sciences, Academia Sinica, Taipei 11529, Taiwan*

<sup>4)</sup>*Leung Center for Cosmology and Particle Astrophysics, National Taiwan University, Taipei 10617, Taiwan*

(\*Electronic mail: [paganis@phys.ntu.edu.tw](mailto:paganis@phys.ntu.edu.tw))

(Dated: 15 October 2024)

This document provides supplementary information of "Dual Mode Superconducting Nanowire Single Photon Detectors".

---

<sup>a)</sup><https://tidc.phys.ntu.edu.tw/>



The SNSPD sample is installed in a cryogenic system, model attoDRY800 from attocube. The temperature is controlled by a heater and the PLC unit of the cryogenic system. The cryogenic system has a minimum temperature of 4.5K and a temperature resolution of  $\pm 0.04\text{K}$  when controlling the sample temperature to higher values. A source meter is used to measure the resistance-current characteristic curve of the SNSPD at different sample temperatures,  $T$ , with bias current,  $I_{bias}$ , in steps of  $0.1 \mu\text{A}$ , as shown in Fig. 1. The Figure displays the resistance-current diagram for the two temperatures utilized in the experiments corresponding to the two SNSPD operation modes. Each marker represents a step of  $0.1 \mu\text{A}$ . While a sharp transition is observed at  $0.39 T_C$ , a setting used for the Geiger mode, for the calorimetric mode setting of  $0.96 T_C$ , a slower transition is observed.

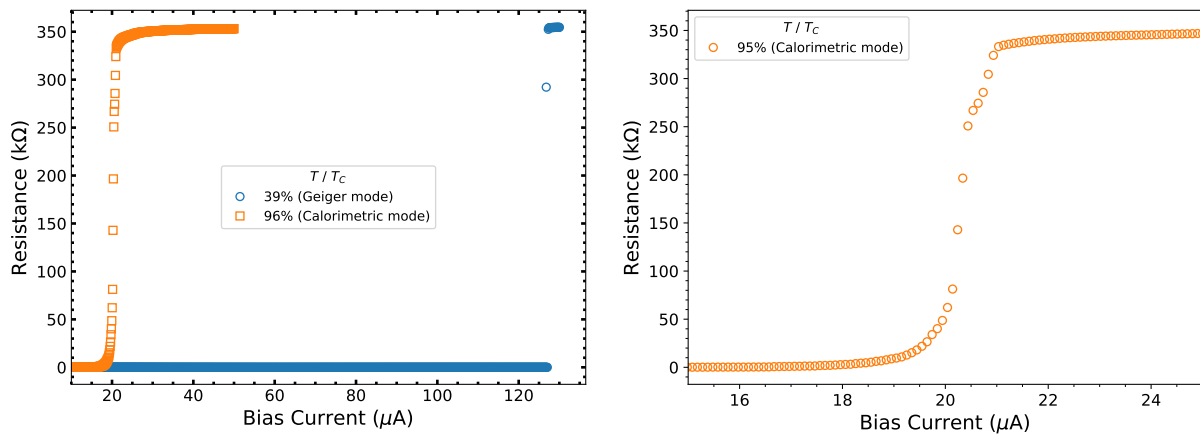


FIG. 1. Resistance-current diagrams for the two different temperature settings employed for the two operation modes of SNSPDs. In the left the curves for operating temperature of  $0.39 T_C$  (Geiger mode) and  $0.96 T_C$  (calorimetric mode) are shown. In the right the superconducting transition is shown for the calorimetric mode in more detail. The marker points represent measurements or resistance in steps of  $0.1 \mu\text{A}$ .

In Fig.2(a) the optical setup for the photoresponse measurements is presented. We utilize a picosecond pulsed laser, Prima from PicoQuant, which has a pulse width of less than 100 ps, a variable repetition rate from 1 kHz to 200 MHz, and three wavelengths: 400 nm, 515 nm, and 640 nm. The source laser beam is collimated into the cryogenic chamber top window (diameter 25 mm, fused silica uncoated) using collimators, mirrors, and beam splitters. The laser beam is then focused using the LT-APO/VIS/0.82 objective lens, which is mounted on the microscope insert directly above the 4K sample holder housing. The objective lens has a numerical aperture (NA) of 0.82, a focal length of 2.87 mm, a working distance of 0.65 mm, an anti-reflection coating in the range of 400-1000 nm, and a magnification of  $100\times$ .

To position the SNSPD sensing region at the focal point, we employ a set of 3-axis ANPx311 piezo-positioners. These piezo-positioners, controlled by the ANC300 modular control unit, offer sub-nanometer fine positioning resolution with a linear positioning range of  $0.8 \mu\text{m}$ . A Charge-Coupled Device (CCD), UI-1240SE-C from IDS Imaging, is employed to capture the reflected light imaging. Additionally, a white light LED is set up in parallel to provide imaging of the pattern. A beam splitter is inserted in the optical path to redirect the reflected light to the CCD. An example image is shown in Fig. 2(b) where the laser spot is focused in the center of the nanowire meander sensing region.

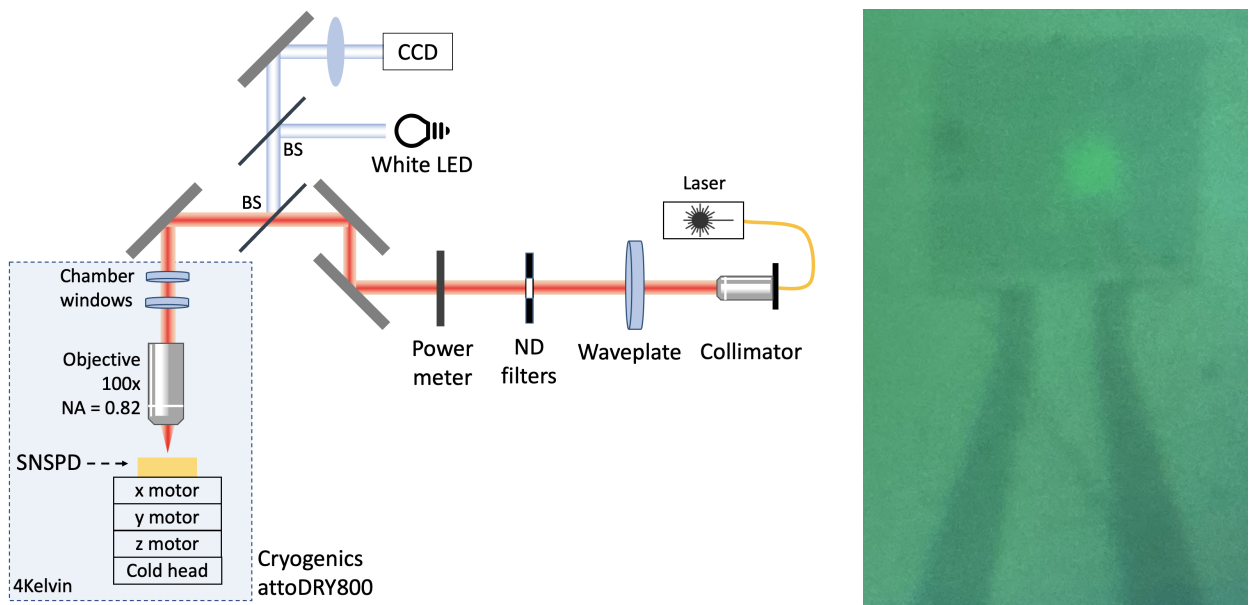


FIG. 2. Schematic of the optical setup (left) and the CCD image of the laser beam positioned in the center of the SNSPD sensing region (right)

For laser-power control, we set up in the optical path a power meter with variable neutral density filters to adjust the laser attenuation level,  $\alpha$ , during measurements. Careful calibration of the light attenuation,  $\alpha_0$ , after the power meter, was conducted prior to the measurements. The attenuation  $\alpha_0$  is kept fixed during the experiments. The mean laser energy per pulse is calculated using the expression  $\frac{P\alpha\alpha_0}{f_{rep}}$ , where  $P$  is the power measured by the power meter and  $f_{rep}$  is the pulse repetition rate. Since the laser polarization also affects the SNSPD absorption, we use a set of polarizers and waveplates to ensure the laser is linearly polarized and the polarization is parallel to the nanowire to get maximum photon absorption

The electronics diagram for the SNSPD signal readout system is shown in Fig. 3. This diagram

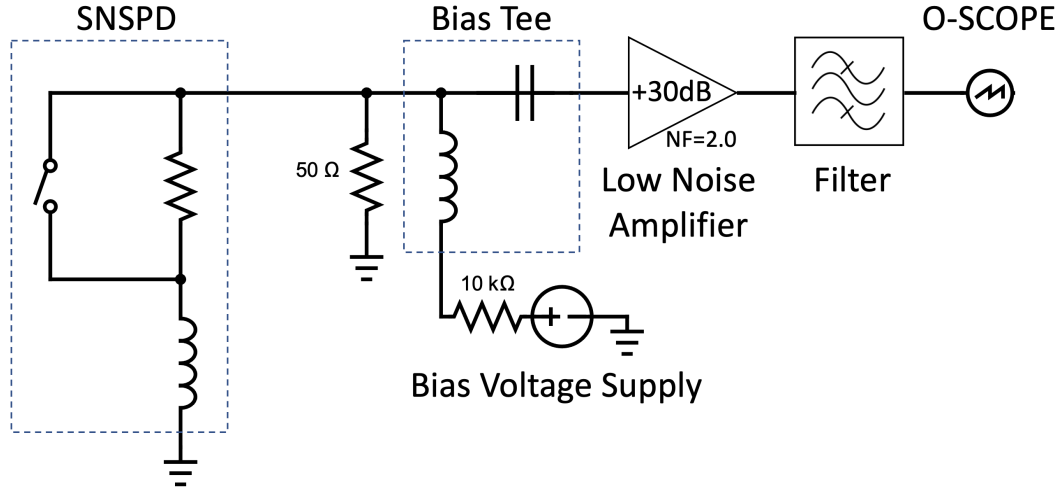


FIG. 3. Electronics diagram for SNSPD signal readout system

illustrates the components and configuration of the electronics used for capturing and digitizing the SNSPD signal. An example of a typical signal and trigger spectrum for a laser pulse event after digitization, is shown in Fig.4. For each event, 1000 samples are recorded, with the trigger arriving at the 300<sup>th</sup> sample and the signal peak arriving at the 325<sup>th</sup> sample, which arrives 25 samples (10 ns) after the trigger. In the pre-signal-pulse region (the first 320 samples), we analyze the baseline characteristics of the noise and signal that yields a mean peak-to-peak noise level of 95 mV, a baseline voltage of 0.2 mV, with a standard deviation of 4 mV. To ensure high-quality data-taking for the final analysis presented in the main paper, we applied pre-selection cuts to reject very noisy events, considering only those with a peak-to-peak noise level greater than 110 mV.

To give an example of the noise influence in the calorimetric mode discussed in the main text, an overlay of SNSPD signal spectra for 100 pulsed-laser events is shown in Fig. 5 (left). The signal spectrum variation for these events highlights the individual pulse characteristics and noise fluctuations, demonstrating a poor signal-to-noise (S/N) ratio, particularly when the signal amplitude is small at low pulsed-laser energies. In contrast, for the average spectrum of 1000 laser pulse events, depicted in Fig. 5 (right), a more consistent and smoother signal profile with a better S/N ratio is observed. By averaging over a larger number of events, the impact of electronic noise is reduced and a clearer representation of the typical SNSPD response to laser pulses is provided.

Figures 6 and 7 show the signal-pulse time constant for different values of  $E_{Laser}$  (left) and  $I_{bias}$  (right), for the Geiger and calorimetric modes, respectively. In the main text, we demonstrate the  $\tau_{fall}$  dependence on  $I_{bias}$  at a fixed  $E_{Laser}$ . The profile plots presented here, show that for both

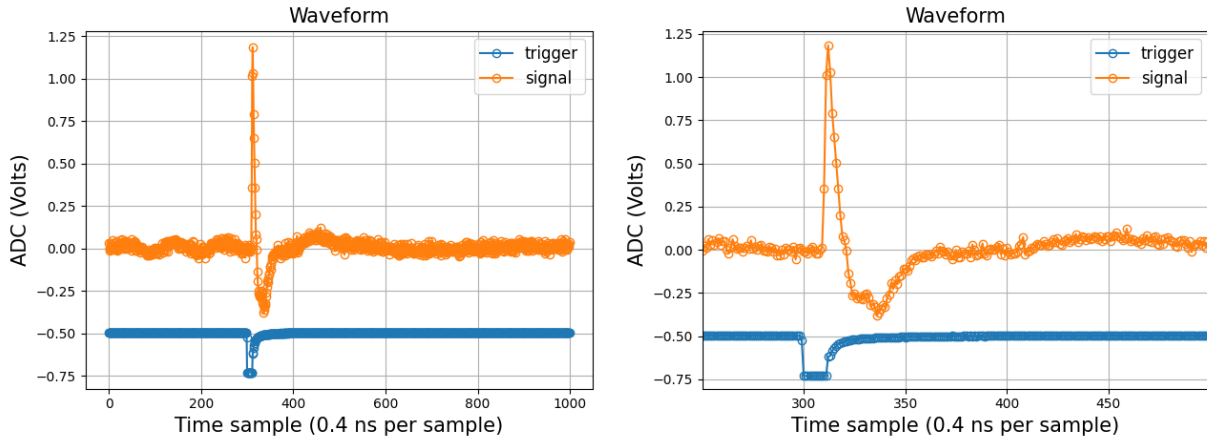


FIG. 4. Example signal and trigger spectra for a single laser pulse event. The x-axis represents the sampling time index, with a sampling interval of 0.4 ns, and a total of 1000 samples recorded for each event. The marker points denote the ADC values of each sample, so the markers have integer x values corresponding to the sampling indices. In the plot, the trigger spectrum is shifted by -0.5 V along the y-axis for clarity. In the right a zoomed-in view of the signal and trigger spectra from time sample 250 to sample 500, is shown.

modes,  $\tau_{fall}$  remains approximately constant across different  $E_{Laser}$  levels, with only a very small remaining dependence.

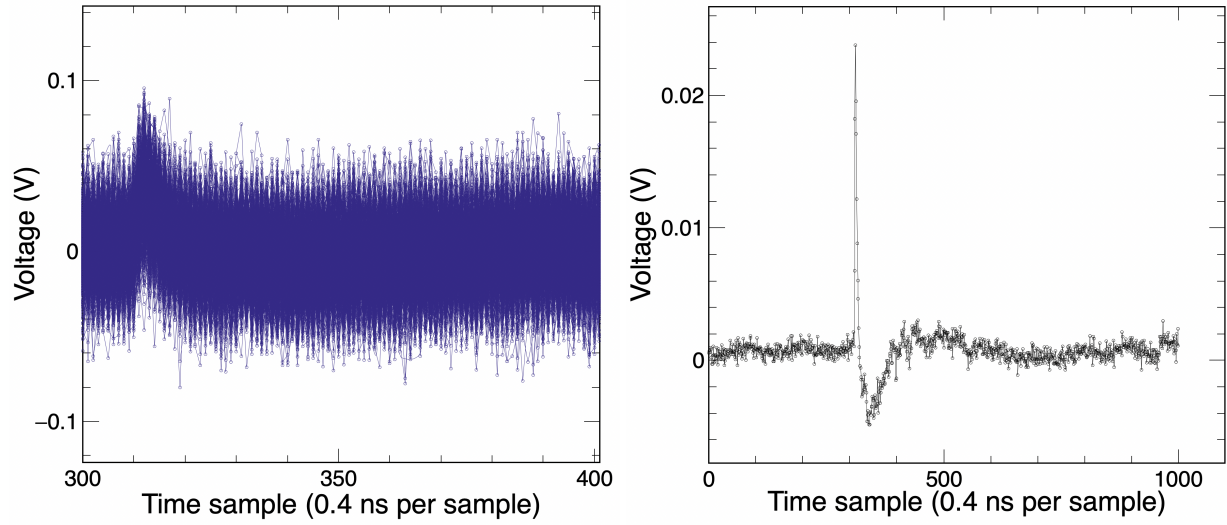


FIG. 5. Left: example overlay of 100 SNSPD output signal spectra from a pulsed-laser source, when the SNSPD is operated in the calorimetric mode at low  $E_{Laser}$ . Right: average signal spectrum of 1000 pulsed-laser events.

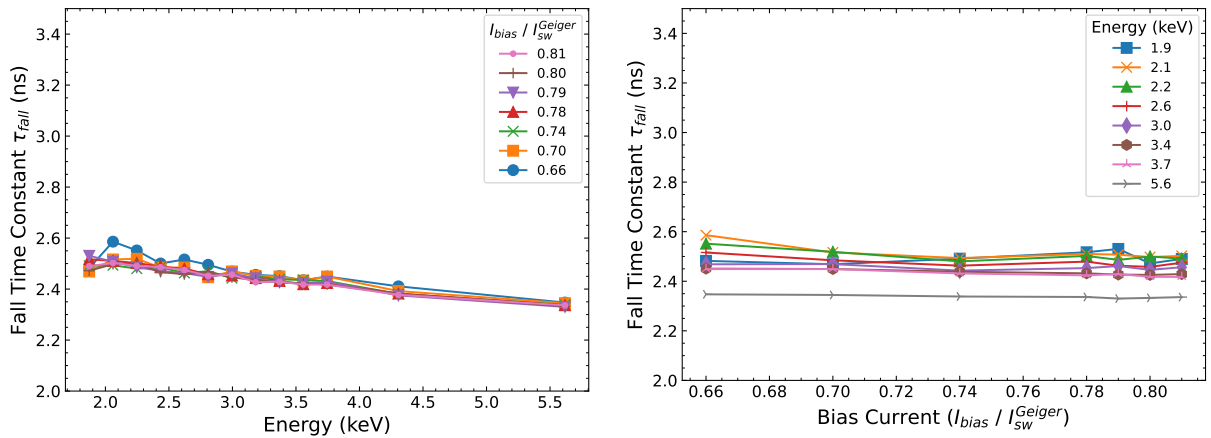


FIG. 6. Geiger Mode: The SNSPD is operated at 4.68K (39%  $T_C$ ). Left: profile of the signal time constant ( $\tau_{fall}$ ) as a function of pulsed-laser energy for different values of  $I_{bias}$ . Right: profile of the signal time constant ( $\tau_{fall}$ ) mean as a function of  $I_{bias}$  for a range of pulsed-laser energies.

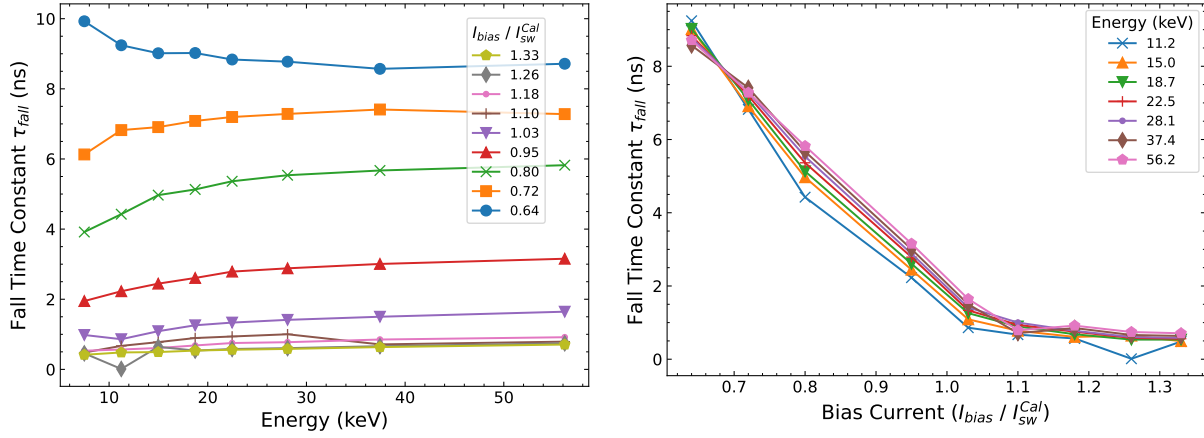


FIG. 7. Calorimetric Mode: The SNSPD is operated at 11.47K (96%  $T_C$ ). Left: profile of the signal time constant ( $\tau_{fall}$ ) as a function of pulsed-laser energy for different values of  $I_{bias}$ . Right: profile of the signal time constant ( $\tau_{fall}$ ) mean as a function of  $I_{bias}$  for a range of pulsed-laser energies.